2022-01

A neural network-based model for lower limb continuous estimation against the disturbance of uncertainty

Li, W

10.1016/j.bspc.2021.103115
Biomedical Signal Processing and Control
Elsevier

A neural network–based model for lower limb continuous estimation against the disturbance of uncertainty

Wanting Li[1], Keping Liu[1,*], Zhongbo Sun[1], Chunxu Li[2], Yuanyuan Chai[1], Jian Gu[1]

1.Department of Control Engineering, Changchun University of Technology, Changchun 130012, PR China

2.Centre for Robotics and Neural Systems, University of Plymouth, Plymouth PL48AA, UK

Abstract

In this paper, a novel prediction model is proposed to estimate human continuous motion intention using a fuzzy wavelet neural network (FWNN) and a zeroing neural network (ZNN). During walking, seven channel surface electromyography (sEMG) signals and motion data of hip and knee are collected, and two signals are selected and processed from the seven muscles based on physiological and correlation analysis. Then, FWNN is built as an intention recognition model, with sEMG signals as input and physical hip and knee information as output. Meanwhile, ZNN is exploited into the FWNN model, forming a hybrid model to eliminate the prediction errors of the FWNN model. Finally, comparative numerical simulations are established to indicate the validity of the FWNN–ZNN model with root mean square error (RMSE), mean absolute error (MAE) and coefficient of determination (R^2) as evaluation indexes. Results show that the proposed FWNN–ZNN model can more accurately estimate human motion intention, which lays the theoretical foundation for the human–robot interaction of rehabilitation robots.

Key words: Neural network, Surface electromyography, Continuous estimation, Correlation analysis, Zeroing neural network

☆The work is supported in part by the National Natural Science Foundation of China under Grants 61873304 and 51875047, and also in part by the Funding of Jilin Province Science and Technology JJKH20210745KJ, and in part by the China Postdoctoral Science Foundation Funded Project under grant 2018M641784, and also in part by the Jilin Engineering Laboratory for Intelligence Robot and Visual Measurement Technology, Grant No. 2019C010.

*Corresponding author.

E-mail addresses: liukeping@ccut.edu.cn (K. P. Liu).

1. Introduction

With the development of signal detection technology, it has become a highly concerned research via sEMG signals to evaluate the activity of neuromuscular in recent years [1–3]. The sEMG is a comprehensive effect of superficial muscle and nerve trunk electrical activity on skin surface, which contains a wealth of information about human behavior. Decoding human behavior information effectively can not only provide a solid theoretical basis for the study of human behavior change law, but also provide effective information for human-computer interaction [4, 5]. The study of sEMG has important practical value in the fields of clinical medicine, biological engineering, sports science and rehabilitation medicine [6–8].

In the field of rehabilitation medicine, the rehabilitation robot is a successful example, and the main research on sEMG is in three aspects. Firstly, sEMG signals are effectively collected and extracted to provide accurate intention recognition [9, 10]. For the multi–classification problem, a two–step supervised learning method is proposed, which can effectively deal with the challenges of weak robustness, insufficient generalization ability and lack of training data in the study of EMG–based hand gesture classification [9]. Second, the simple and optimized interactive control method is designed for the robot [11–13]. In [11], a solar–powered wheelchair is designed, which employs the intention recognized by the adaptive neuro–fuzzy system from the sEMG signals as the control input of the wheelchair. The third aspect, muscle activity is utilized to evaluate human physiological indicators and the auxiliary effects of wearable robot [14–16]. In order to ameliorate the efficiency of clinical evaluation, a fuzzy logic–based method is displayed to automatically assess the impairment degree of stroke patients via sEMG signals [14]. In particular, the precise intention recognition based on sEMG is the premise of completing the other two studies. Thus, intention recognition based on sEMG is the focus of research in the field of rehabilitation medicine, which needs to be studied intensively. Commonly, there are two types of continuous motion intention recognition methods, including muscle model and regression model. The basic framework of the muscle model is the joint dynamics model, in which the input is sEMG signals and the output is the joint posture, angular velocity, joint torque. As a muscle model, hill–based muscle model (HMM) is widely applied in motor intention estimation [17, 18]. [17] combines joint dynamics and HMM to establish a state-space model for continuous motion estimation. Considering generalization, the synthesized maximum normalization is designed in order to eliminate the dependence of prediction model on different external loads. It is crucial to accurately identify the HMM parameters for motion intention recognition. However, it is difficult to construct the HMM for practical application owing to some physiological parameters that cannot be directly measured. On the other

hand, the regression model is constructed between the sEMG signals and joint motion information to predict human motor intention, among which neural network is the most commonly applied [19–22]. In [19], continuous wavelet transform integrated into back propagation neural network is proposed to estimate the continuous motion intention of the upper limb via the sEMG signals under human-robot interaction, but the correlation between the selected muscles and the recognized movements is not considered. In [20], an improved fuzzy neural network is applied to the elbow joint angle estimation, and the feasibility of this method is proved by comparative experiments. To estimate the posture of the upper limb in continuous motion, the SCA-LSTM algorithm is proposed, which reduces noise interference by custom maximum root mean square envelope preprocessing method [21]. Nevertheless, the linear processing mode of long short–term memory leads to an increase in prediction time, which hinders online application in human–robot interaction.

Unavoidably, there are non–ideal conditions in sEMG signals acquisition, such as skin sweating, electrode movement and electrode shedding, which will reduce the accuracy of intention recognition. The interactive system is a key solution to this problem, which eliminates this interference while retaining useful information. For discrete motion estimation, [23] developers a myoelectric pattern recognition based on adaptive incremental hybrid classifier, which improved the robustness of myoelectric pattern recognition against interference and has been proved by experiments. [24] adopts information fusion technology by integrating multiple sensors to improve the prediction accuracy of upper limb motion intention, but the algorithm complexity is increased. Nevertheless, this problem has not been thoroughly discussed in the identification of lower limb continuous motion intention. The traditional regression model has disadvantages, such as strong randomness, error accumulation and unable to eliminate interference, which leads to large forecasting errors. In addition, the network parameters of the neural network are excessively dependent on the training set. In other words, it is easy to cause the prediction error once the test data and training data are different. However, the closed–loop system is essential to overcome these problems. ZNN has exponential convergence in the framework of a closed–loop system, which can be introduced into the estimation model to eliminate errors [25–27]. In [25], the ZNN model is comprehensively interpreted, with the core idea being the construction of an error function. Besides, a noise–tolerant zeroing neural network model is proposed considering the nonlinear system with various noises [28–31]. [31] surmounts the disadvantage that traditional solvers can only handle static problems. The effectiveness and advancement of the two discrete–time ZNN models proposed from both theoretical and numerical perspectives are proved by taking a planar four–link manipulator as an example.

In this paper, a novel prediction model combining FWNN and ZNN, named as the FWNN–ZNN model, is developed to estimate lower limb motor intention by sEMG signals. The salient points are summarized as follows. First, the muscles associated with hip and knee joints are selected during walking according to physiology and correlation analysis. Further, by analyzing the stability and convergence of ZNN, the FWNN–ZNN model is utilized to eliminate the prediction error in the FWNN model for the uncertain influence in the forecasting process. Finally, the availability and superiority of the FWNN–ZNN model is verified by comparative experiments with the FWNN model.

This paper is arranged as follows. Section 2 introduces the collection, processing and selection of experimental data. In Section 3, by analyzing the stability and convergence of ZNN, a novel neural network-based method via ZNN and FWNN is developed for the estimation of lower limb motion intention. Section 4 characterizes the performance of the FWNN–ZNN model by analyzing and comparing experimental results. Section 5 presents a summary and outlook.

2. Experimental

2.1. Signal acquisition

The purpose of this experiment is to estimate hip and knee angles during human walking based on sEMG from leg muscles. Figure 1 shows the muscle distribution of the left lower limb. The thigh muscles are divided into anterior, posterior and medial groups [32]. The muscles of the anterior group are dominated by the femoral nerve, which mainly controls hip flexion and knee flexion-extension. The anterior group includes sartorius (SR), rectus femoris (RF) and lateral femoral (LF). The muscles in the posterior group are innervated by the sciatic nerve, mainly controlling hip extension and knee flexion. The posterior group consists of biceps femoris (BF), semitendinosus (ST) and semimembranous (SM). The medial group was not studied because the muscles in the medial group controlled hip adduction and external rotation.

All the muscles in the calf muscles control foot movement except for the gastrocnemius (GM), which controls knee flexion. As a result, sEMG of seven muscles including SR, RF, LF, BF, ST, SM and GM are recorded at a frequency of 2,000 Hz via the MP160 system (BIOPAC Systems Inc., American), as presented in Figure 2. Simultaneously, hip and knee joint angles are sampled by a gyroscope sensor (Wit Motion Co. Ltd., China) with a 100 Hz sampling rate to supply real-time data during walking, as shown in Figure 2.

The experimental scenario is illustrated in Figure 2. An able-bodied subject (male, 25 years old, 1.75 m, 65 kg) is invited to participate in the experiment. The

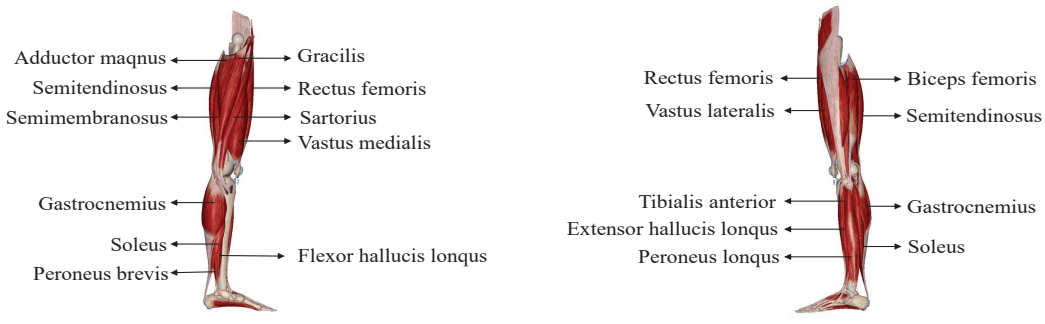

(a)The left view. (b)The right view.

Figure 1: The muscle distribution of the left lower limb.

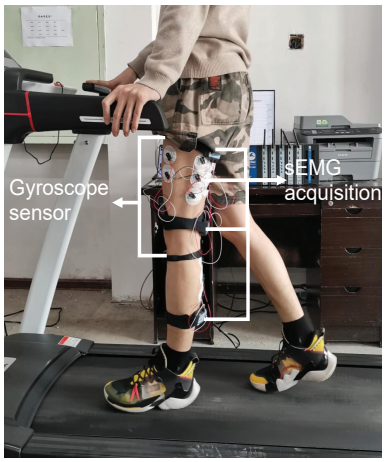

Figure 2: The experimental scenario.

equipment for data acquisition is worn on the subject's left limb to collect sEMG signals and joint angles while the subject walks on the treadmill. Disposable gel electrodes, attached to the muscles, are recommended by sEMG for the non-invasive assessment of muscles guidelines [33]. The electrode has the advantages of strong adsorption and is difficult to shift, but the signal acquisition principle makes the collected signal easy to introduce adjacent muscles crosstalk [34]. Therefore, it is crucial to determine the position and method of sticking the electrodes that will affect the accuracy of continuous motion estimation. Electrodes are attached to each muscle in pairs, about 2 cm apart (centre to centre). In particular, hair and skin keratin are not cleaned in order to improve the practicality of the proposed method. Figure 3 demonstrates the collected primary sEMG signals. The acquired joint motion information is introduced in Figure 4.

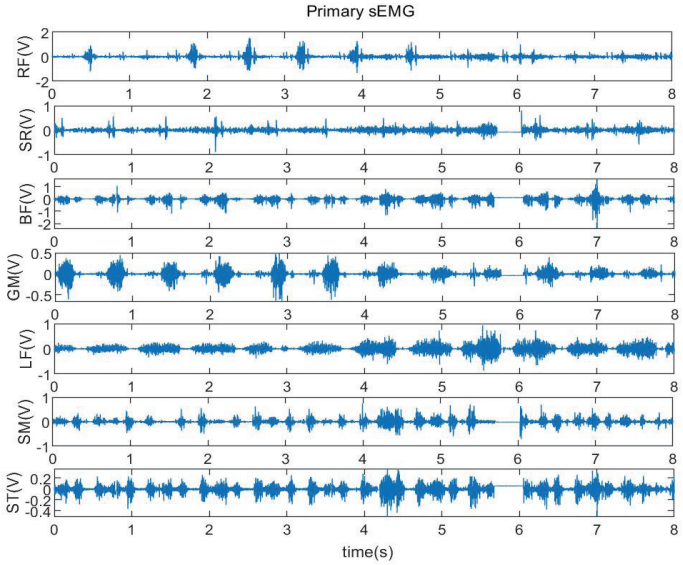

Figure 3: The collected sEMG signal.

2.2. Signals processing

The acquired sEMG signals are weak signals and contain a variety of noises, which can easily make the sEMG signals distortion. First, the sEMG signals collected from the skin surface are inevitably influenced by physical factors such as hair, sebum, and cross–talk from adjacent muscles. Moreover, the sEMG signals are also affected by the electrode cables and power frequency interference during the acquisition process. The noises make the acquired signals vibrate violently, which will affect the accuracy

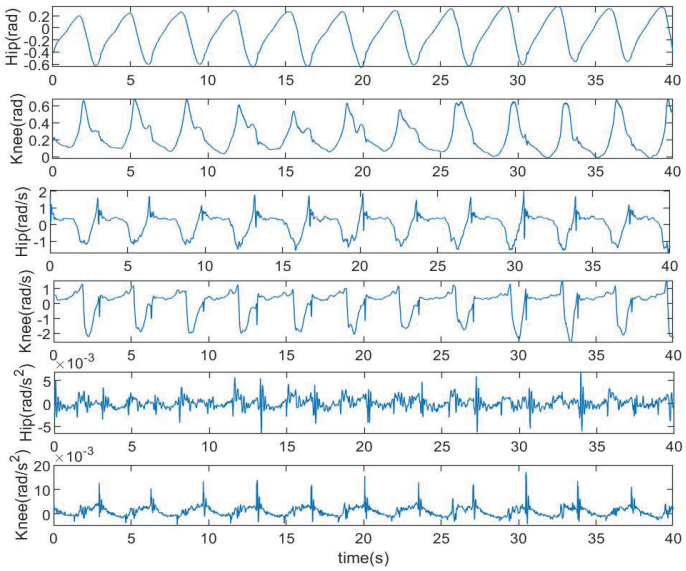

Figure 4: The angle, angular velocity and angular acceleration of joints are collected.

of the estimation. The sEMG power spectrum is mainly concentrated at 20–50 Hz. Consequently, a band–pass filter and a notch filter (50 Hz) are necessary to eliminate the noises from the primary sEMG signals. The primary sEMG signals after simple noise elimination are named the preprocessed sEMG signals.

The preprocessed sEMG signals have frequent oscillations and random amplitudes. To solve the problem, the digital processing of sEMG signals is carried out by a full–wave rectification method. The process can be done by:

$$\mathrm{sEMG}_r(n) = |\mathrm{sEMG}_p(n)| \tag{1}$$

where $\mathrm{sEMG}_p(n)$ is the nth amplitude of the preprocessed sEMG signals, $\mathrm{sEMG}_r(n)$ is the nth amplitude sample of the signals though full–wave rectification, as shown in Figure 5.

The sampling frequency of the gyroscope sensor is 100 Hz, while the sampling frequency of sEMG acquisition equipment is 2000 Hz. The sEMG signals need to be sub-sampled to ensure the input and output of the model are one-to-one mapping. The sub-sampling can be expressed as

$$\mathrm{sEMG}_{sub}(n) = \frac{1}{N} \sum_{i=nN-N+1}^{nN} \mathrm{sEMG}_r(i) \tag{2}$$

where N is the time of sub–sampled required for the signals, $\mathrm{sEMG}_{sub}(n)$ is the

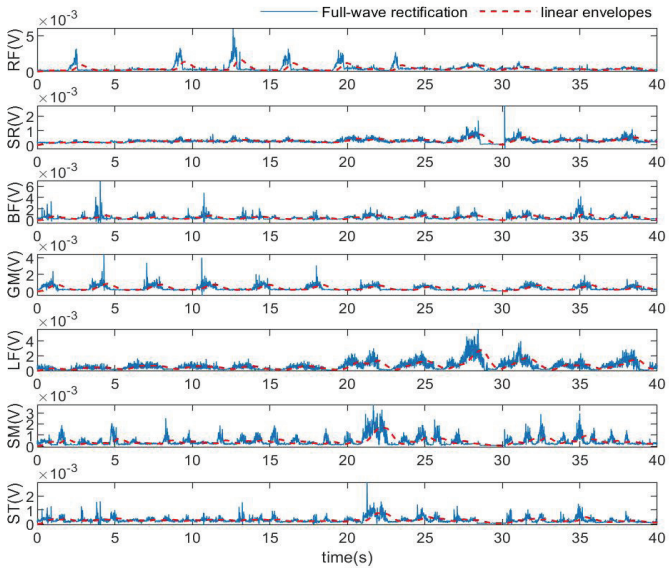

Figure 5: The collected sEMG signals are subjected to full-wave rectification and linear envelopes.

signals through sub–sampling. Considering the real–time performance, the Butterworth filter is adopted for low-pass filtering of the signals. The transfer function of the Butterworth filter adopted is:

$$G^2(\omega) = |H(j\omega)|^2 = \frac{G_0^2}{1 + \left(\frac{\omega}{5}\right)^4}, \tag{3}$$

where G_0 is the DC gain. This filters out individual peaks, resulting in a smooth linear envelope that reflects the magnitude of sEMG activity. Hereby, the linear envelopes of signals are obtained and described in Figure 5. In the final stage, the linear envelopes are normalized to the interval [0,1], which are treated as input parameters for the estimation model.

2.3. Correlation analysis

There are many muscles associated with hip and knee movements in the lower limbs. It is necessary to explore the correlation between muscles and moving joints during walking. Finding the muscles most related to hip and knee motion can better carry out the prediction experiment and obtain more valuable results for estimating lower limb motion intention.

Correlation analysis is a statistical method to study whether there is such an uncertain relationship between things or phenomena. CC is a variable that reflects

the degree of linear correlation between variables. According to the different research objects, CC is divided into simple CC, multiple CC and typical CC. It is a time series analysis to estimate lower limb motor intention based on sEMG signals, in which the relationship between sEMG signals and joint angles is non-deterministic. In this paper, the simple CC is utilized to analyze the correlation between sEMG signals and joint angles to find the most suitable muscles for the prediction experiment, which is defined as

$$\mathrm{CC_s} = \frac{\mathrm{Cov}(x, y_{\mathrm{pre}})}{\sqrt{\mathrm{Var}(x)\mathrm{Var}(y_{\mathrm{pre}})}}, \tag{4}$$

where x represents the normalized linear envelope of sEMG signals, y_{pre} denotes the joint angle, $\mathrm{Cov}(x, y_{\mathrm{pre}})$ is the covariance of x and y_{pre}, $\mathrm{Var}(x)$ and $\mathrm{Var}(y_{\mathrm{pre}})$ are the variances of X and y_{pre}, respectively.

Table 1: Correlation analysis between sEMG signals and joint angles.

	ST	SM	GM	SR	BF	LF	RF
$\mathrm{Angle_{hip}}$	0.2432	0.0343	0.1983	0.1875	0.6009	0.2771	0.0444
$\mathrm{Angle_{knee}}$	0.3677	-0.0145	0.8182	-0.1502	0.3670	0.4073	-0.3943

Correlation analysis between sEMG signals and joint angles is demonstrated in Table 1. Generally, the greater the CC, the stronger the relationship between the sEMG signals and joint angles, the better the prediction effect. As it can be seen, CC(BF, $\mathrm{Angle_{hip}}$) and CC(GM, $\mathrm{Angle_{knee}}$) are the values with the highest correlation between sEMG signals and joint angles. Hereby, the estimation accuracy of lower limb motion intention can be improved by selecting sEMG of BF and GM as the input of prediction.

2.4. Skeletal dynamics model

Based on motion anatomy, the force generated by muscle contraction causes the connected joints to produce torque, which pulls the bone and creates joint movement. It is essential to establish the dynamic equation of the lower limb to study the change of joint motion information during human walking. A skeletal dynamics model of the lower limb is established considering only the motion of the hip and knee joints around the frontal axis, which represents the relationship between joint torque and joint angular velocity. Figure 6 displays the lower limb skeleton.

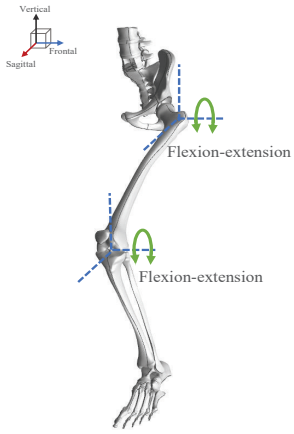

Figure 6: Skeleton model of the left leg.

Based on the Lagrangian–Euler formulation, skeletal dynamics model of the left leg can be reformulated as

$$M\left(q\right)\ddot{q}+C\left(q,\dot{q}\right)\dot{q}+G\left(q\right)=\tau_{m}, \tag{5}$$

where M is the inertia matrix, C denotes the centripetal and coriolis, q, $\dot{q}$ and $\ddot{q}$ indicate the angle, angular velocity and angular acceleration of joints, G is the gravity matrix, τ_m is the torque applied on joints.

Accordingly, the relationship between angular velocity and torque can be expressed as

$$\begin{cases} \dot{q}_1 = q_2, \\ \dot{q}_2 = -M^{-1}\left[C\left(q_1,\dot{q}_1\right)\dot{q}_1 + G(q_1)\right] + M^{-1}\tau_m, \end{cases} \tag{6}$$

where q_1 and q_2 represent the angle and angular velocity of joints.

3. Neural network–based model

3.1. FWNN model

Continuous motion recognition based on sEMG signals is challenging because of its limited datasets, strong randomness, and difficult modeling. In this section, the wavelet function and adaptive fuzzy neural network (AFNN) are combined to form the FWNN to estimate lower limb motor intention. In this fuzzy system, the relationship between sEMG signals and joint information values is interpreted as decipherable fuzzy rules. FWNN combines the advantages of fuzzy logic, wavelet

function and neural network, which can quickly and accurately estimate the continuous motion of lower limbs. Wavelet functions aim to replace the linear functions in the THEN part in order to improve the computing ability and computing time of the fuzzy system. AFNN integrates the wavelet function into the IF–THEN rule, which belongs to the Takagi–Sugeno–Kanag type with high learning accuracy, and is expressed as:

$$\begin{aligned} R^i\text{: if } x_1 \text{ is } A_1^i\text{, and } x_2 \text{ is } A_2^i\text{, } \ldots\text{,and } x_r \text{ is } A_r^i\text{,} \\ \text{then} \quad y_i = \omega_j \sum_{j=1}^{r} \psi_{ij}\left(x_j\right), \end{aligned} \tag{7}$$

where x_j is the j-dimensional input variable of rule i, $j = 1, 2, \ldots, r$,$i = 1, 2, \ldots, n$ is the number of rules, y_j and ω_i are the output and weight coefficients of rule i, A_j^i denotes the membership function of input, ψ_{ij} is obtained by stretching and shifting the wavelet mother function. It is defined as:

$$\psi_{ij}(x_j) = [1 - (\frac{1}{b_{ij}}(x_j - a_{ij}))^2]\exp\frac{-(x_j - a_{ij})^2}{2b_{ij}^2}. \tag{8}$$

Figure 7 introduces the structure of FWNN. To reduce the complexity of the model, a simplified adaptive fuzzy reasoning system is applied to the model.

Layer 1: Input layer, which brings external data into network without information processing.

Layer 2: Membership function layer. The number of nodes is obtained by subtraction clustering algorithm. Gaussian function is selected, as shown in Equation (9):

$$A_j^i(x_j)\exp\frac{-(x_j - a_{ij})^2}{2b_{ij}^2}. \tag{9}$$

Layer 3: The fuzzy inference layer calculates the excitation intensity of each rule. To simplify structure, the fuzzy rules and membership functions have the same number. The output of the jth node is:

$$\mu_j = \prod_{j=1}^{r} A_j^i(x_j). \tag{10}$$

Layer 4: The normalized layer, which aims to normalize the nodes of the previous layer. The output is:

$$\overline{\mu_j} = \frac{\mu_j}{\sum_{j=1}^{n} \mu_j}. \tag{11}$$

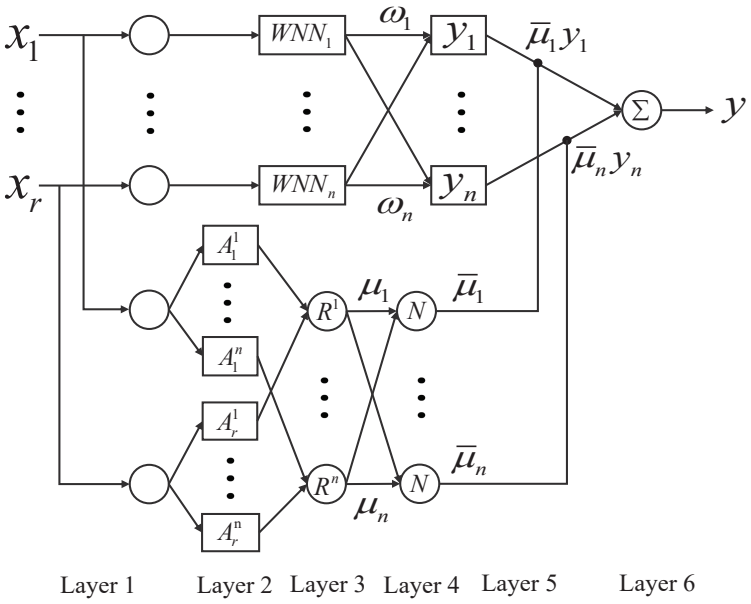

Figure 7: Structure of FWNN.

Layer 5: Regular output layer, whose output is:

$$W_j = \overline{\mu_j} y_j. \tag{12}$$

Layer 6: Network output layer, the output is the sum of all the rule output.

$$y = \sum_{j=1}^{n} W_j. \tag{13}$$

FWNN model is designed to estimate joints angles and angular velocites via sEMG signals. Normalized envelopes of sEMG signals are taken as the input of the model, which can be defined as:

$$x_i = [x_{i,1}, \ldots, x_{i,s}], \quad s = 1, 2, \quad i = 4000, \tag{14}$$

where s represents sEMG of BF and GM. The acquired data are taken as the expected output,

$$y_{\text{exp}} = [y_{1,j}, \ldots, y_{i,j}], \quad j = 1, \ldots, 6, \tag{15}$$

where j represents joint angle, angular velocity and angular acceleration of two joints. The output of FWNN can be defined as:

$$y_{\text{pre}} = [y_{1,j}, \ldots, y_{i,j}], \quad j = 1, \ldots, 6. \tag{16}$$

3.2. ZNN

The motion intention by the FWNN model is an open–loop system as visualized in Figure 8. In general, the open-loop system without automatic correction capability results in increased prediction errors. The errors, such as assumptions about physiological parameters, simplification of models and noise between sensors, will lead to inaccurate estimates of lower limb motor intention. However, the effect of cumulative error is able to be effectively eliminated by the closed-loop method.

ZNN has exponential convergence, which is derived from recurrent neural network [27]. ZNN aims to construct an error function, such as making the prediction error of the FWNN model approach zero. In [28, 29], the zero–finding problem is defined as follow:

$$g(y(t), t) = 0 \in R^{n\times n} \, , t \subseteq [0, +\infty) \, , \tag{17}$$

where $y(t) \in R^{n\times n}$ is the real time variable, $g : R^{n\times n} \times [0, +\infty) \to R^{n\times n}$ is the nonlinear time-varying mapping function. Since the solution $y^*(t)$ of zero–finding problem exists at $t \subseteq [0, +\infty)$, the error function is expressed as:

$$E(t) = g(y^*(t), t) - g(y(t), t) = 0 - g(y(t), t). \tag{18}$$

In addition, the problem (17) and (18) can be transformed into the classical nonlinear dynamical model

$$\begin{cases} \dot{y} = u(t), \\ \psi(t) = g(y(t), t) = -E(t), \end{cases} \tag{19}$$

where $y(t)$ represents the time-varying state variable, $u(t)$ and $E(t)$ are the input function and output function of a nonlinear dynamic model. Therefore, the error function is designed to be $\dot{E}(t) = -\lambda E(t)$ and a set of $n \times n$ decoupled differential equations is equivalently generalized as

$$\dot{e}_{i,j}(t) = -\lambda e_{i,j}(t), \tag{20}$$

where $i, j \in \{1, 2, 3, ..., n\}$, $\lambda > 0$ is related to the rate of convergence.

Theorem 1: When the error function $e_{i,j}(t)$ satisfies (20), the state variable $y(t)$ of nonlinear dynamic system (19) globally and exponentially converges to $y^*(t)$, the control law can be generalized as

$$u(t) = -\left(\frac{\partial g(y(t), t)}{\partial y}\right)^{-1} \left(\lambda \cdot g(y(t), t) + \frac{\partial g(y(t), t)}{\partial t}\right). \tag{21}$$

Proof: From formula (20), the Lyapunov function candidate can be defined as

$$\nu_{i,j}(t) = \frac{e_{i,j}^2(t)}{2} \geqslant 0. \tag{22}$$

The time derivative of formula (22) can be written as

$$\dot{\nu}_{i,j}(t) = \frac{d\nu(t)}{dt} = e_{i,j}(t)\,\dot{e}_{i,j}(t) = -\lambda e_{i,j}^2(t) \leqslant 0. \tag{23}$$

According to Lyapunov theory, as time t tends to infinity, starting from any $e_{i,j}(0)$, $e_{i,j}(t)$ globally asymptotically stable and exponentially converges to zero with a rate $\lambda > 0$. Further, by substituting Equation (20) into Equation (19), the following implicit formula is obtained:

$$\xi(y(t),t)\dot{y}(t) = -\lambda(g(y(t),t)) - \frac{\partial g(y(t),t)}{\partial t} \tag{24}$$

The control law (21) can be obtained by substituting Equation (24) into classical nonlinear dynamic system (19).

3.3. FWNN–ZNN model

The accuracy of intention recognition can be improved by introducing a ZNN–based closed-loop system into the prediction model. When the predicted values deviate from the expected values in the closed-loop system, the corresponding control function will be gained to eliminate the error. Hence, the closed-loop system has the characteristics of reducing interference and enhancing the ability of model prediction. The structure of the FWNN–ZNN model is introduced in Figure 8.

Based on equation (5), the total torque $\tau_{F,i}$ estimated by the FWNN model can be expressed as

$$\tau_{F,i} = M(q_{1,i})\,\ddot{q}_{1,i} + C(q_{1,i}, q_{2,i})\,q_{2,i} + G(q_{1,i}), \tag{25}$$

where $q_{1,i}$, $q_{2,i}$ and $\dot{q}_{2,i}$ respectively represent the predicted joint angle, angular velocity and angular acceleration predicted by the FWNN model.

According to the dynamic equation, the above equation can be converted into:

$$\begin{cases} \dot{q}_{1,i} = q_{2,i}, \\ \dot{q}_{2,i} = -M^{-1}\left[C(q_{1,i}, \dot{q}_{1,i})\,\dot{q}_{1,i} + G(q_{1,i})\right] + M^{-1}\tau_{F,i}. \end{cases} \tag{26}$$

The nonlinear dynamic model (19) is discretized by first-order Euler difference, and combined with the FWNN model (26), the FWNN–ZNN model can be expressed as follow:

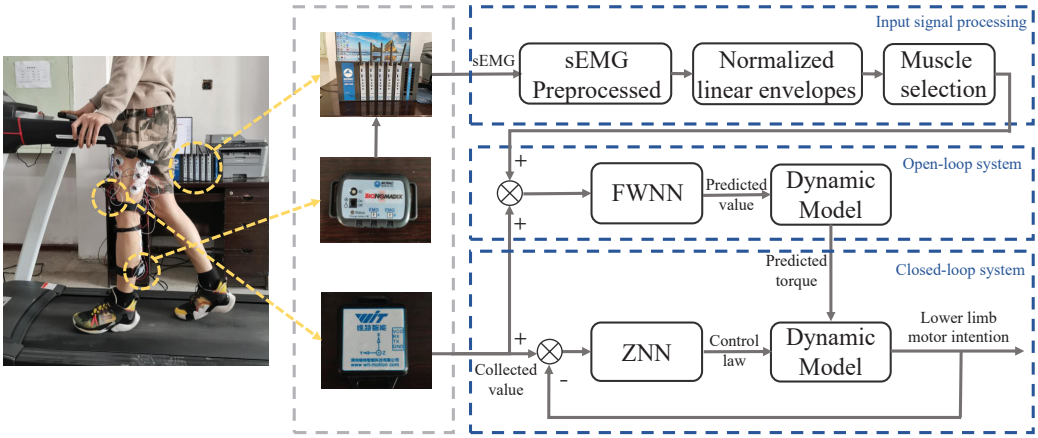

Figure 8: Flowchart of motion intention estimation.

$$\begin{cases} q_{k+1} = q_k + \dot{q}_k T_s, \\ \dot{q}_{k+1} = g(q_k, t_k) + u(t_k), \end{cases} \tag{27}$$

where T_s is the sampling time, $q_k = [q_{i,k}; \dot{q}_{i,k}]$ denotes the time-varying state variable. The $g(q_k, t_k)$ can be described as

$$g(q_k, t_k) = [q_{2,i,k}; -M^{-1}\left[C\left(q_{1,i,k}, \dot{q}_{1,i}\right)\dot{q}_{1,i,k} + G(q_{1,i,k})\right] + M^{-1}\tau_{i,k}], \tag{28}$$

Let $e(t_k) = q_{d,k} - q_k$, combining the equation (21) and discrete time technique. Here, $q_{d,k} = [q_1; q_2]$ in equation is the desired state variable, the controller can be described as

$$u_{ZNN}(t_k) = \dot{q}_{d,k} + \gamma(q_{d,k} - q_k) - g(q_k, t_k). \tag{29}$$

The ZNN controller (29) provides the control framework to deal with the convergence and robustness of the time series prediction model, which improves the accuracy of motion intention recognition.

4. Results and analyses

To demonstrate the feasibility of the proposed FWNN–ZNN model, the continuous motion estimation experiment of the lower limb is established based on the sEMG signals and joint information. Keeping all parameters unchanged, the experiment is randomly set in triplicates to avoid accidental phenomena and make the results more reliable. In addition, the estimation experiments of the FWNN model are utilized

to form comparative experiments, which explore the superiority of the FWNN–ZNN model.

Simulation experiments are implemented via Matlab. The 4000 data points extracted are divided equally into two parts, and the model performance is trained and tested. Combinating with Table 2 and Figures 9–12, the properties of the two estimation models are discussed. To broadly evaluate the models' performance, three indicators RMSE, MAE and R^2 are exploited to calculate the prediction accuracy of the two models. RMSE can be expressed by the following formula:

$$\mathrm{RMSE} = \sqrt{\frac{1}{2000}\sum_{i=1}^{2000}\left\|y_{\exp}(i) - y_{\mathrm{pre}}(i)\right\|_2^2}. \tag{30}$$

MAE can be written as follows

$$\mathrm{MAE} = \frac{1}{n}\sum_{i=1}^{n}\left|y_{\exp} - y_{\mathrm{pre}}\right|. \tag{31}$$

R^2 can be defined as

$$R^2 = 1 - \frac{\sum_{i=0}^{n}\left(y_{\exp} - y_{\mathrm{pre}}\right)^2}{\sum_{i=0}^{n}\left(y_{\exp} - \bar{y}_{\exp}\right)^2}, \tag{32}$$

where $\bar{y}_{\exp}$ is the average of the expected output.

The performance values of three randomized experiments are introduced in Table 2. The closer the R^2 value is to 1, the better the estimated performance of the model. However, for RMSE and MAE, the closer the value is to 0, the better the prediction performance of the model. From Table 2, it can be intuitively shown that the FWNN–ZNN model has better indicators, that is, better prediction performance. It proved the validity of the established skeletal dynamics model and the feasibility of the FWNN–ZNN prediction model. Moreover, the corresponding performance values are essentially agreed based on the FWNN–ZNN model in the three groups of simulation experiments. In this paper, continuous motion estimation of lower limbs can be regarded as a nonlinear problem. Since ZNN (21) has high accuracy and strong robustness for solving nonlinear problems, FWNN–ZNN model (28) has strong inhibition performance for uncertain factors. The discretization degree of sample error can be evaluated by combining RMSE and MAE. Specifically, the larger the difference between RMSE and MAE, the higher the dispersion degree of sample error. This bias is mainly present in the prediction of angular velocity, especially based on the FWNN model. Furthermore, the prediction effect of angular velocities

Table 2: Evaluation of the predicted results under different models.

	Part	RMSE		MAE		R^2	
		FWNN	FWNN–ZNN	FWNN	FWNN–ZNN	FWNN	FWNN–ZNN
#1	$\text{Angle}_{\text{hip}}$	0.1224	0.0071	0.0820	0.0048	0.8308	0.9994
	$\text{Angle}_{\text{knee}}$	0.0803	0.0118	0.0587	0.0084	0.8213	0.9964
	$\text{Angle velocity}_{\text{hip}}$	0.3259	0.1544	0.2557	0.0734	0.7342	0.9463
	$\text{Angle velocity}_{\text{knee}}$	0.4976	0.1721	0.3578	0.1150	0.6284	0.9620
#2	$\text{Angle}_{\text{hip}}$	0.1204	0.0071	0.1014	0.0048	0.7807	0.9994
	$\text{Angle}_{\text{knee}}$	0.0794	0.0118	0.0624	0.0085	0.8556	0.9964
	$\text{Angle velocity}_{\text{hip}}$	0.3260	0.1544	0.2445	0.0730	0.7250	0.9463
	$\text{Angle velocity}_{\text{knee}}$	0.4975	0.1731	0.3432	0.1147	0.6583	0.9615
#3	$\text{Angle}_{\text{hip}}$	0.1278	0.0071	0.0936	0.0048	0.8135	0.9994
	$\text{Angle}_{\text{knee}}$	0.0843	0.0118	0.0559	0.0085	0.8549	0.9964
	$\text{Angle velocity}_{\text{hip}}$	0.3341	0.1544	0.2344	0.0720	0.6522	0.9465
	$\text{Angle velocity}_{\text{knee}}$	0.5321	0.1705	0.3495	0.1145	0.8186	0.9623

is worse than angles in the three experiments, and this phenomenon is more obvious in the prediction experiments of the FWNN model. This phenomenon reflects that the FWNN–ZNN model has a low requirement for sample stability and strong robustness.

In more detail, the superiority of the FWNN–ZNN model is analyzed with the first group of experiments as an example. The predicted results of the first experiment are described in Figures 9–12. In Figures 9–12, black solid lines represent the raw data, while orange dotted lines and pink dashed lines represent the predicted results of the FWNN model and FWNN–ZNN model, respectively.

Figure 9 shows the comparison of the raw angle data with the estimated value. It can be seen that the dashed line representing the FWNN–ZNN model is highly coincident with the solid line representing the original value, while the dotted line is oscillating. For the FWNN model, the prediction effect is disappointing at the curve wave peak. For example, the dotted prediction of hip deviates significantly from the solid line at 5–6s but only slightly at 7–8s. The FWNN model adopts the gradient correction method to adjust the network weight and the parameters of the wavelet basis function, which leads to the inevitable phenomenon. From Table 2, the RMSE of predicting hip and knee angles using the FWNN–ZNN model is 0.0071 and 0.0118, which are both lower than the FWNN model, while the R^2 of predicting hip and knee angles utilizing FWNN–ZNN model is 0.9994 and 0.9964, which are

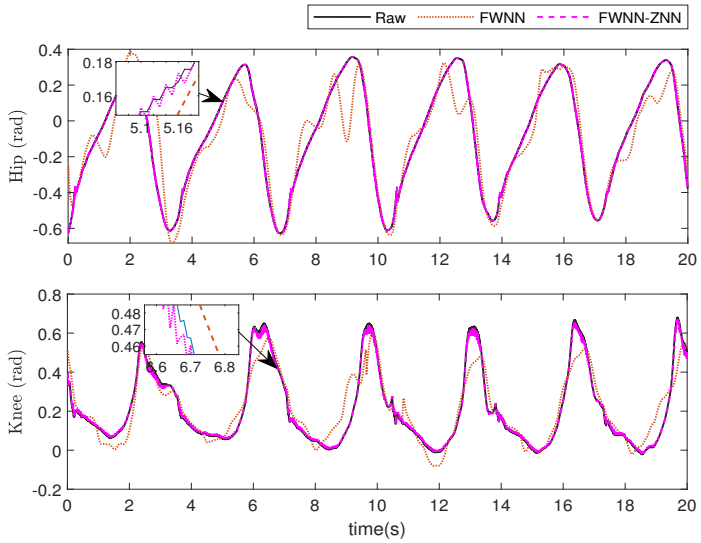

Figure 9: Compare the raw angle data with the estimated value.

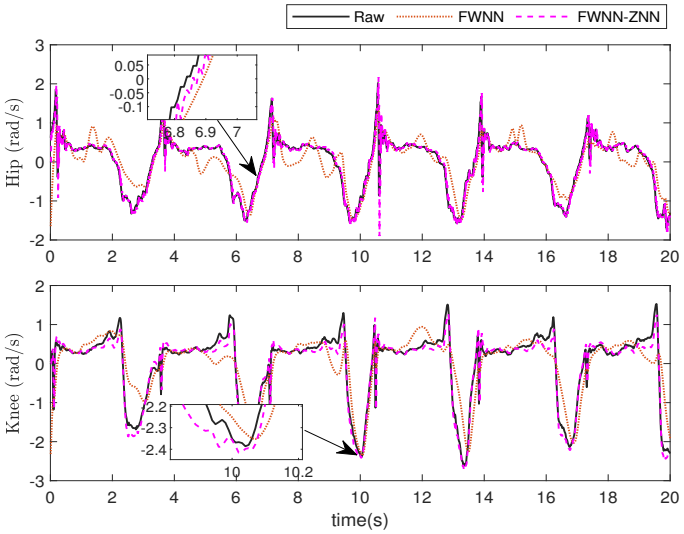

Figure 10: Compare the raw angular velocity with the estimated value.

both higher than the FWNN model. Figure 10 illustrates the comparison of the raw angular velocity with the estimated value. Similarly, the prediction effect of the FWNN–ZNN model for angular velocity is better than that of the FWNN model. It indicates that the FWNN–ZNN model based on ZNN is advanced and can effectively improve the prediction precision.

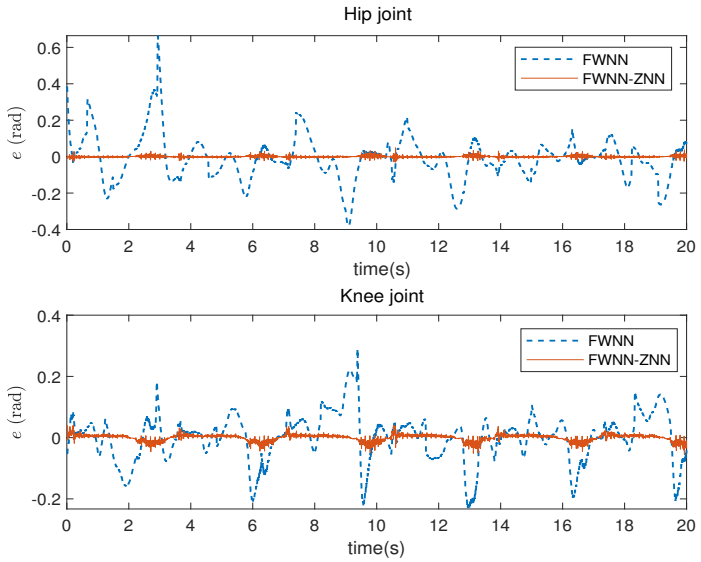

Figure 11: The angle errors of the two estimation models.

Figures 11–12 depicts the joint angle and angular velocity errors of two estimation models, where blue dashed and orange solid lines represent the prediction errors of the FWNN model and the FWNN–ZNN model. As observed, the estimation errors of the FWNN model are able to be effectively reduced by introducing the ZNN model. However, it is worth noting that the prediction effect of the FWNN model for angular velocity is weaker than that of joint angle. Uncertainties in the modeling process of the FWNN model result in differences, such as the periodicity of original data samples and the randomly initialized wavelet factors, which can affect the accuracy of estimation. From Figures 10, it can be seen that the original angular velocity curves have many oscillations. The large fluctuation of the original angular velocity values is also reflected in the difference between RMSE and MAE in Table 2. This phenomenon indicates that the prediction of FWNN model depends on the raw data, whereas the FWNN–ZNN model does not. It fully illustrates that the constructed error function (20) can effectively eliminate errors caused by randomness and indeterminacy in the FWNN model and improve the prediction accuracy. It is

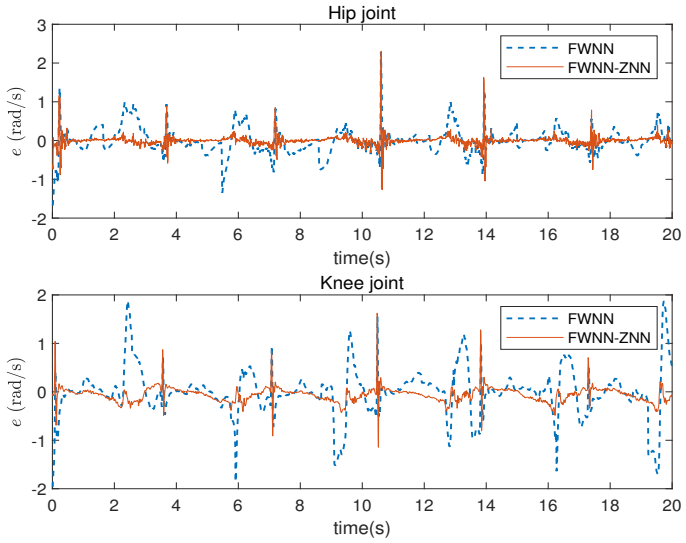

Figure 12: The angular velocity errors of the two estimation models.

further proved that the proposed FWNN–ZNN model is stable and superior.

The prediction time of the model is also the criterion to evaluate the model's performance. The prediction time of the FWNN–ZNN model is about seven times that of the FWNN model, in which the FWNN–ZNN model takes 54.2166s and the FWNN model takes 7.8091s. The complex structure of the FWNN–ZNN model increases the prediction time. However, in this experiment, the model is established to estimate lower limb motor intention under off-line conditions, so the prediction speed is not strictly required.

The evaluation indicates that the FWNN–ZNN model has strong uncertainty rejection performance, which greatly reduces the influence brought by uncertain factors. The proposed model can be effectively applied to practical work, for instance, biomedical engineering, clinical medicine, human–robot information interaction.

5. Conclusions

In this paper, a novel prediction model formed by FWNN and ZNN has been designed to predict humans walking on the treadmill based on sEMG signals. A healthy man has been invited to complete a walking experiment in which seven sEMG signals and two joint data have been collected from his left leg. Correlation analysis has been made between the normalized linear envelopes extracted from the sEMG signals and the angle data of two joints, and two muscles with high CC have

been selected as the input of the prediction model. By comparative experiments, the overall performance of the FWNN–ZNN model has been better than the FWNN model, which proves the proposed prediction model has strong robustness to the uncertain factors and can be extended to practical application.

In fact, real–time online intention recognition is more widely applied in biological engineering, which requires high precision and speed of model prediction. The next work focuses on collecting clinical data from patients for motor intention recognition, improving the performance of the estimation model and applying the intention recognition algorithm combined with human-robot interaction control to the actual lower limb exoskeleton robot.

References

[1] P. Wei, J. H. Zhang, F. F. Tian and J. Hong, A comparison of neural networks algorithms for EEG and sEMG features based gait phases recognition, Biomedical Signal Processing and Control. 68(2021) 102587.

[2] H. Urbanek, V. D. Smagt, iEMG: Imaging electromyography, Journal of Electromyography and Kinesiology. 27(2016) 1–9.

[3] A. Sandberg, The standard concentric needle cannula cannot replace the Macro EMG electrode, Clinical Neurophysiology. 125(2014) 406–410.

[4] C. X. Li, C. G. Yang and C. Giannetti, Segmentation and generalisation for writing skills transfer from humans to robots, Cognitive Computation and Systems. 1(2019) 20–25.

[5] C. X. Li, C. G. Yang, J. Wan, A. Annamalai and A. Cangelosi, Neural learning and kalman filtering enhanced teaching by demonstration for a baxter robot, 2017 23rd International Conference on Automation and Computing (ICAC), Huddersfield, UK. (2017) 1–6.

[6] K. Z. Zhuang, N. Sommer, V. Mendez, S. Aryan, E. Formento, E. D'Anna, F. Artoni, F. Petrini, G. Granata, G. Cannaviello, W. Raffoul, A. Billard and S. Micera, Shared human–robot proportional control of a dexterous myoelectric prosthesis, Nature Machine Intelligence. 1(2019) 400–411.

[7] G. Wang, Y. B. Liu, T. Shi, X. Q. Duan, K. P. Liu, Z. B. Sun and L. Jin, A novel estimation approach of sEMG–based joint movements via RBF neural network, 2019 Chinese Automation Congress (CAC), Hangzhou, China. (2019) 1783–1788.

[8] A. Vijayvargiya, C. Prakash, R. Kumar, S. Bansal and J. M. R.S. Tavares, Human knee abnormality detection from imbalanced sEMG data, Biomedical Signal Processing and Control. 66(2021) 102406.

[9] G. Y. Jia, H. K. Lam, S. C. Ma, Z. H. Yang, Y. J. Xu and B. Xiao, Classification of electromyographic hand gesture signals using modified fuzzy c–means clustering and two–step machine learning approach, IEEE Transactions on Neural Systems and Rehabilitation Engineering. 28(2020) 1428–1435.

[10] Y. Y. Chai, K. P. Liu, C. X. Li, Z. B. Sun, L. Jin and T. Shi, A novel method based on long short term memory network and discrete–time zeroing neural algorithm for upper-limb continuous estimation using sEMG signals, Biomedical Signal Processing and Control. 67(2021) 102416.

[11] M. S. Kaiser, Z. I. Chowdhury, S. A. Mamun, A. Hussain and M. Mahmud, A neuro-fuzzy control system based on feature extraction of surface electromyogram signal for solar–powered wheelchair, Cognitive Computation. 8(2016) 946–954.

[12] H. Liu, J. Tao, P. Lyu and F. Tian, Human–robot cooperative control based on sEMG for the upper limb exoskeleton robot, Robotics and Autonomous Systems. 125(2020) 103350.

[13] F. Nougarou, A. Campeau–Lecours, D. Massicotte, M. Boukadoum, C. Gosselin and B. Gosselin, Pattern recognition based on HD–sEMG spatial features extraction for an efficient proportional control of a robotic arm, Biomedical Signal Processing and Control. 53(2019) 101550.

[14] L. Liparulo, Z. Zhang, M. Panella, X. D. Gu and Q. Fang, A novel fuzzy approach for automatic Brunnstrom stage classification using surface electromyography, Medical & Biological Engineering & Computing. 55(2017) 1367–1378.

[15] G. Chen, P. Qi, Z. Guo and H. Y. Yu, Mechanical design and evaluation of a compact portable knee–ankle–foot robot for gait rehabilitation, Mechanism and Machine Theory. 103(2016) 51–64.

[16] S. Tecco, V. Quinzi, A. Nota, A. Giovannozzi, M. R. Abed and G. Marzo, Electromyography–guided adjustment of an occlusal appliance: Effect on pain perceptions related with temporomandibular disorders. A Controlled Clinical Study, Diagnostics. 11(2021) 1–11.

[17] J. D. Han, Q. C. Ding, A. B. Xiong and X. G. Zhao, A state–space EMG model for the estimation of continuous joint movements. IEEE Transactions on Industrial Electronics. 62(2015) 4267–4275.

[18] D. Ao, R. Song and J. Gao, Movement performance of human–robot cooperation control based on EMG–driven hill–type and proportional models for an ankle power–assist exoskeleton robot, IEEE Transactions on Neural Systems and Rehabilitation Engineering. 25(2017) 1125–1134.

[19] Y. J. Huang, K. B. Chen, X. M. Zhang, K. Wang and J. Ota, Motion estimation of elbow joint from sEMG using continuous wavelet transform and back propagation neural networks. Biomedical Signal Processing and Control. 68(2021) 102657.

[20] Y. B. Liu, C. X. Li, Z. W. Teng, K. P. Liu, G. Wang and Z. B. Sun, Intention recognition of elbow joint based on sEMG using adaptive fuzzy neural network, 2020 5th International Conference on Mechanical, Control and Computer Engineering (ICMCCE), Harbin, China. (2020) 1091–1096.

[21] C. F. Ma, C. Lin, O. W. Samuel, L. S. Xu and G. L. Li, Continuous estimation of upper limb joint angle from sEMG signals based on SCA-LSTM deep learning approach, Biomedical Signal Processing and Control. 61(2020) 102024.

[22] C. Wang, W. Y. Guo, H. Zhang, L. L. Guo, C. C. Huang and C. Lin, sEMG-based continuous estimation of grasp movements by long-short term memory network, Biomedical Signal Processing and Control. 59(2020) 101774.

[23] Q. C. Ding, X. G. Zhao, J. D. Han, C. G. Bu and C. D. Wu, Adaptive hybrid classifier for myoelectric pattern recognition against the interferences of outlier motion,muscle fatigue, and electrode doffing, IEEE Transactions on Neural Systems and Rehabilitation Engineering. 27(2019) 1071–1080.

[24] S. Jiang, Q. H. Gao, H. Y. Liu and P. B. Shull, A novel, co–located EMG–FMG–sensing wearable armband for hand gesture recognition, Sensors and Actuators A: Physical. 301(2020) 111738.

[25] Y. N. Zhang, F. Li, Y. W. Yang and Z. Li, Different Zhang functions leading to different Zhang–dynamics models illustrated via time–varying reciprocal solving, Applied Mathematical Modelling. 36(2012) 4502–4511.

[26] L. Jin, S. Li, B. Hu, M. Liu and J. G. Yu, Noise–suppressing neural algorithm for solving time–varying system of linear equations: a controlbased approach, IEEE Transactions on Industrial Informatics. 15(2019) 236–246.

[27] L. Jin, S. Li and B. Hu, RNN models for dynamic matrix inversion: a control-theoretical perspective, IEEE Transactions on Industrial Informatics. 14(2018) 189–199.

[28] L. Jin, Y. N. Zhang, S. Li and Y. Y. Zhang, Modified ZNN for timevarying quadratic programming with inherent tolerance to noises and its application to kinematic redundancy resolution of robot manipulators, IEEE Transactions on Industrial Electronics. 63(2016) 6978–6988.

[29] Z. B. Sun, T. Shi, L. Wei, Y. Y. Sun, K. P. Liu and L. Jin, Noise–suppressing zeroing neural network for online solving time–varying nonlinear optimization problem: a control–based approach, Neural Computing and Applications. 32(2020) 11505–11520.

[30] L. Jin, Y. Zhang, S. Li and Y. Zhang, Noise–tolerant ZNN models for solving time–varying zero–finding problems: a control–theoretic approach, IEEE Transactions on Automatic Control. 62(2017) 992–997.

[31] Z. B. Sun, Y. B. Liu, L. Wei, K. P. Liu, L. Jin and L. Q. Ren, Two DTZNN models of pattern for online solving dynamic system of linear equations: application to manipulator motion generation, IEEE Access. 8(2020) 36624–36638.

[32] F. Polak. Gait analysis: An introduction. Physiotherapy, 2009.

[33] D. A. Winter. Biomechanics and motor control of human movemen. University of Waterloo Press, 2009.

[34] R. Baker. Measuring walking: A handbook of clinical gait analysis richard baker. Mac Keith Press, 2013.